Medium-Length Lipids Facilitate Cell-Permeability and Bioactivity

Johannes Morstein*[a,b], Alice Capecchi[c,#], Konstantin Hinnah[d,#], Jerome Petit-Jacques[e],
Jean-Louis Reymond[c], Dirk Trauner[b]

[a] Department of Cellular and Molecular Pharmacology and Howard Hughes Medical Institute,
University of California, San Francisco, California 94158, USA
[b] Department of Chemistry, New York University, New York, New York 10003, USA
[c] Department of Chemistry and Biochemistry, University of Bern, Freiestrasse 3, 3012 Bern,
Switzerland
[d] Department of Chemical Biology, Max Planck Institute for Medical Research, Jahnstrasse 29,
69120 Heidelberg, Germany
[e] NYU School of Medicine, Ion Lab, 435 East 30th Street, New York, New York 10016, USA
*Johannes.Morstein@ucsf.edu

Abstract

The majority of bioactive molecules act on membrane proteins or intracellular targets and therefore needs to partition into or cross biological membranes. Natural products often exhibit lipid modifications to facilitate critical molecule-membrane interactions and in many cases their bioactivity is markedly reduced upon removal of a lipid group. However, despite its importance in nature, lipid-conjugation of small molecules is not commonly used in chemical biology and medicinal chemistry, and the effect of such conjugation has not been systematically studied. To understand the composition of lipids found in natural products, we carried out a chemoinformatic characterization of the 'natural product lipidome'. According to this analysis, lipidated natural products predominantly contain saturated linear medium-length lipids, which are significantly shorter than those found in membranes and lipidated proteins. To study the usefulness of such modifications in probe design, we systematically explored the effect of lipid conjugation on five different small molecule chemotypes and find that permeability, cellular retention, subcellular localization, and bioactivity can be significantly modulated depending on the type of lipid tail used. We demonstrate that medium-length lipid tails can render impermeable molecules cell-permeable and switch on their bioactivity. Saturated medium-length lipids (e.g. C10) are found to be ideal for the bioactivity of small molecules in mammalian cells, while saturated long-chain lipids (e.g. C18) often significantly reduce bioavailability and activity. Together, our findings suggest that conjugation of small molecules with medium-length lipids could be a powerful strategy for the design of probes and drugs.

Introduction

To function within a membrane or cell, small molecules need to be actively or passively transported into or across biological membranes. The physicochemical properties allowing for both membrane permeability and aqueous solubility are thought to be tightly confined.[1–3] Strikingly, nature and medicinal chemistry vary in their approaches for the synthetic design of highly bioactive molecules (Figure 1). With a few notable exceptions of amphiphilic probes and pharmacophores, including fingolimod (FTY720),[4] eliglustat,[5] palmostatin B,[6] salmeterol,[7] and orlistat,[8] synthetic small molecule probes and pharmacophores rarely exhibit lipid tails. Natural products, on the other hand commonly exhibit lipid functionalizations that fine-tune their pharmacokinetic and/or pharmacodynamic properties. Well known examples include bryostatin,[9,10] thapsigargin[11], daptomycin,[12] and phorbol ester[13]. In addition to membrane permeability, direct drug-membrane interactions play key roles in targeting proteins that are embedded in or associated with biological membranes.[14–16] These include G protein-coupled receptors (GPCRs), receptor-linked enzymes, ion channels, transporters, pumps, and many transiently membrane localized proteins (e.g. RAS, PI3K, PKC), which together represent the majority of known drug targets.[17] In the case of transmembrane proteins, lipophilic drugs can enter a target directly through lateral diffusion from the intermembrane space of the lipid bilayer, as has been recently established for a number of endogenous and synthetic GPCR and ion channel ligands.[16,18,18–23] The prevalence of lipidated natural products, and some notable examples of amphiphilic endogenous ligands, synthetic probes, and pharmacophores, as well as the fundamental tenet that the vast majority of drugs interact in critical ways with biological membranes poses many pressing questions. While the lipid composition of biological membranes[24,25] and the posttranslational modifications of proteins with lipid groups[26,27] have been major fields of research, the systematic conjugation of lipids to small molecules and the composition of lipidated natural product are largely unexplored.[28] Here, we present a systematic characterization of the lipid composition of lipidated natural products through chemoinformatics, as well as a survey of the effects of lipid conjugation on several classes of small molecules.

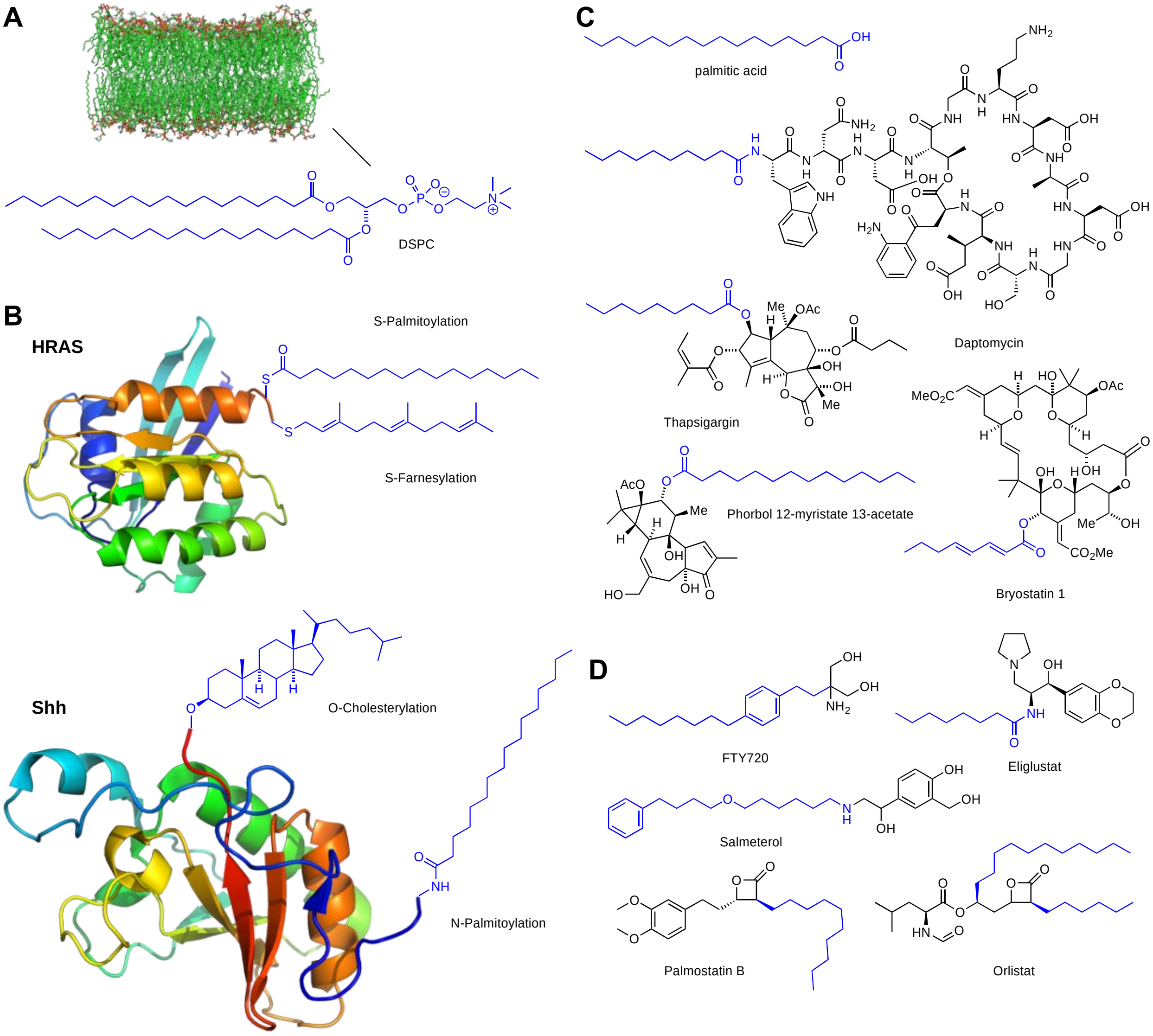

Figure 1 | Lipid occurrences in nature and pharmacology. (A) Biological membrane with major lipid component distearoylphosphatidylcholine (DSPC). (B) Selection of proteins that undergo posttranslational lipidation. HRAS (PDB 5P21[29]) and Shh (PDB 3N1R[30]). (C) Selection of lipidated natural products. (D) Selection of lipidated synthetic chemical probes and approved drugs.

Results

Chemoinformatic Characterization of the ‘Natural Product Lipidome’

Lipid-functionalization of small molecules occurs very commonly in nature. Many natural products are lipidated, and their bioactivity is often significantly reduced when the lipid tail is altered or removed.[9,11,13] To systematically study how widespread this modification is and what type of lipids are most prevalent, we sought to characterize lipidated natural products (Figure 2A). For our search, we turned to the COlleCtion of Open Natural prodUcTs (COCONUT)[31], which is an open-source database of over 400,000 elucidated and predicted natural products. Our analysis focused only on the 67,656 COCONUT entries annotated with a taxonomical origin and a publication DOI. Of these, the majority are of plant origin (50%), followed by fungal (23%), bacterial (16%), homo sapiens (2.5%), animal (2%), and marine (1.5%) origin.[32] The remaining 5% lack a superclass annotation, and it was annotated as “other”. To define a lipidated subset among the 67,656 unique natural products, we selected those with an uninterrupted hydrocarbon chain of at least eight atoms. Then, in order to exclude classical lipids (e.g. glycolipids, sphingolipids, and sterols), we further confined our search to molecules exhibiting at least one closed ring that is not a sugar and excluded molecules that have a molecular weight lower than 200 Da without the lipid tail, or exhibit a sterol substructure. Through such filters and manual curation, we identified 1,308 lipidated natural products.

To allow an overview of the 67,656 selected COCONUT entries and of the lipidated subset, all structures were encoded in the MAP4 (MinHashed atom pair fingerprint of diameter 4)[33] feature space and visualized in an interactive manner using TMAP (TreeMap)[34]. The MAP4 fingerprint combines the characteristics of atom pair fingerprints, which are well suited for large molecules and peptides, and substructure fingerprints, which are instead preferred for small molecules, and it is therefore suitable for both. TMAP is a dimensionality reduction method suitable for analyzing vast high-dimensional datasets used in combination with the 3D visualization tool Faerun.[35] The obtained map is available at https://tm.gdb.tools/map4/lipidatedNP_tmap/, and it can be used to visualize the lipidated NPs subset among the 67,656 COCONUT entries (Figure 2B). Additionally, the map can be navigated using Molecular weight (MW), fraction of sp3 C (Fsp3), hydrogen bond donors (HBD) and acceptors (HBA) count, the estimated octanol:water partition coefficient (AlogP), the presence/absence of peptide and sugar moieties, compliance with Lipinski's rules of five,[36] based on origin of the NPs, and the presence or absence of glycoside and peptide substructures (Figure S1).

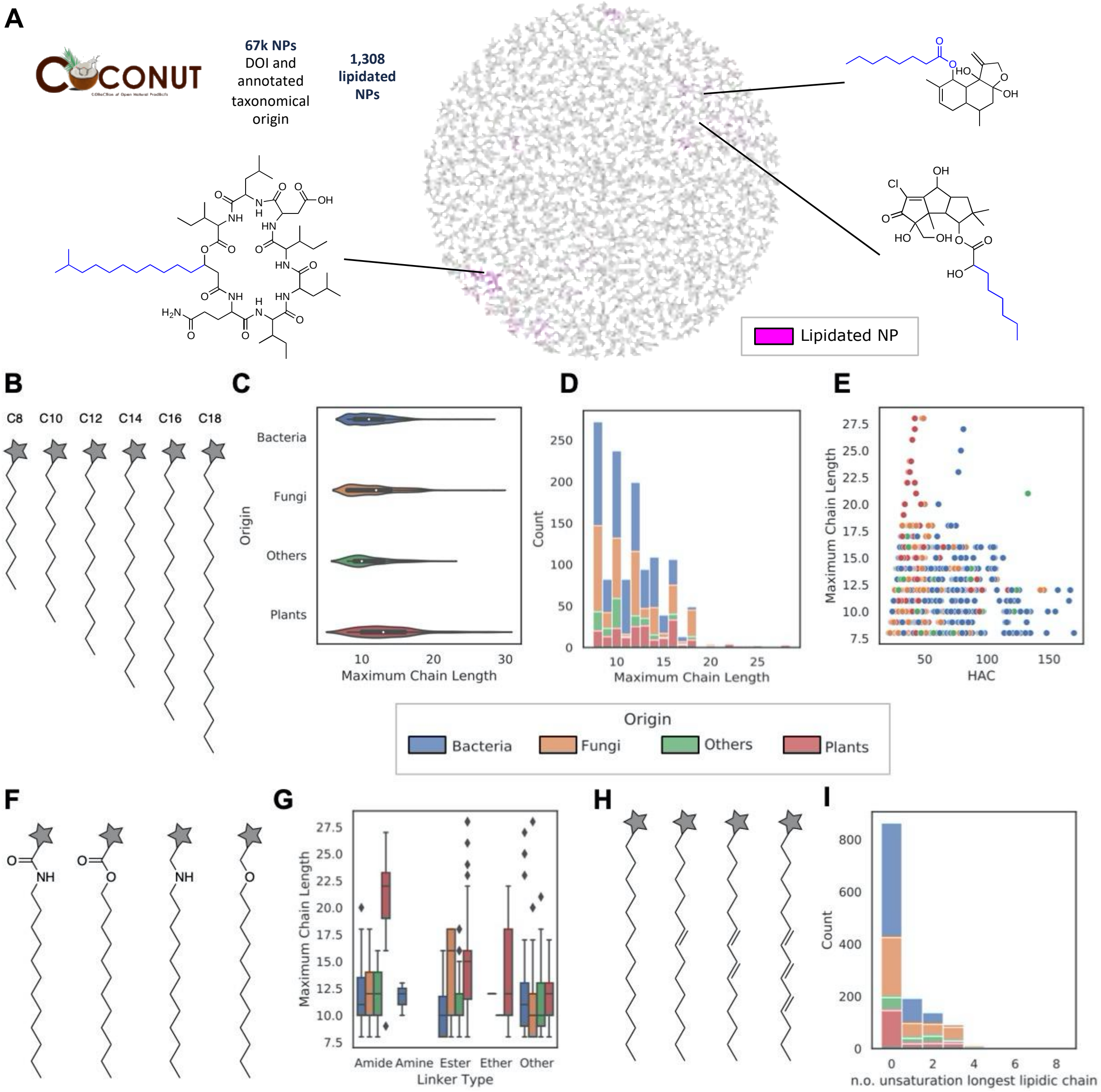

Figure 2 | Chemoinformatic characterization of ‘Natural Product Lipidome’. (A) Graphical depiction of lipidated natural products within COCONUT database. (B) Examples of lipid chain structures with varying lengths. (C) Lipid chain length distribution in natural products with various origins (violin plot). (D) Counts of lipid chain lengths distribution in natural products with various origins (stacked histogram). (E) Correlation of lipid chain length with HAC parameters of lipidated natural products (scatter plot). (F) Examples of lipid chain structures with varying connecting functional groups. (G) Chain length distribution across the different lipid connecting functional groups in natural products with various origins (box plot). (H) Examples of lipid chain structures with varying

degrees of saturation. (I) Count of lipids in natural products with varying degrees of saturation and origin (stacked histogram).

To characterize the natural product lipidome, we conducted several analyses of the identified hits. These include the distribution of lipid chain length (Figure 2B-D), correlation with hydrogen bond acceptor count (HAC) (Figure 2E), the distribution of connecting functional groups (Figure 2F-G), and the occurrence of varying degrees of saturation (Figure 2H-I). Since the lipidated NPs subset contained only 20 human NPs, 20 marine NPs, and two animal NPs, we have grouped these three classes with the 84 lipidated NPs missing a superclass annotation under the label “other”. Notably, we found that the lipid tail lengths in natural products across different origins (animal, bacteria, fungi, and plants) exhibit a similar trend in length distribution in being predominantly significantly shorter than lipid groups used in the functionalization of proteins or as constitutional components of biological membranes.[37,38] Correlation with the functional group connector of the lipid tails shows that the chain length is not strongly correlated with a particular type of connecting group. Finally, our analysis shows that unsaturation is not uncommon, but most lipid chains are fully saturated. These finding suggested that medium-length lipid tails were well suited for bioactive molecules. To investigate this point closer, we set out to prepare a series of fluorophore-lipid conjugates and study their cellular uptake and distribution.

Cellular Uptake of Fluorophore-Lipid Conjugates

To study the capability of lipids to mediate cellular uptake of non-permeable small molecules, we synthesized a series of lipidated fluorescein thiourea conjugates from fluorescein isothyiocyanate (FITC) through treatment with various aminolipids (Figures 3A). Fluorescein exhibits low intrinsic cell permeability and has been used extensively to assess new mechanisms for cellular uptake, including thiol-mediated uptake[39,40] or cell-penetrating peptide mediated uptake.[41–43] Cellular uptake of lipidated fluorescein derivatives was assessed in HeLa cells through live cell fluorescent imaging (Figure 3B). Strikingly, large differences were found in intracellular fluorescence after a short (15 min) treatment of live cells with the respective lipid-fluorescein conjugate (Figure 3C and D). Very short tails in **1** (C2) and **2** (C6) did not mediate significant cellular uptake, while conjugates with longer saturated tails showed a >100 times increase in cellular fluorescence. **3** (C10), **4** (C14), and **5** (C18) showed strong plasma membrane localized fluorescence, but notably **3** and **4** also exhibit fluorescence localized to endomembranes indicative of cellular uptake. It is unclear if **5** was bound to the inner leaflet of the plasma membrane or associated with cells on the outer leaflet of the cell membrane. Conjugate **10** also exhibited strong plasma membrane localized fluorescence. Strikingly, all other lipid structures explored did not mediate strong association with the plasma membrane. These data suggests that the capacity to associate with the plasma membrane is correlated with the conformational flexibility and not molecular weight or overall lipophilicity. Other lipid structures also enabled significant cellular uptake (e.g. **6**, **8**, **9**, and **12**), while highly structurally confined types of lipids (**7** and **11**) including a sterol-derived structure appeared unable to mediate rapid plasma membrane association or cellular uptake. To provide further evidence that these effects are not primarily based on lipophilicity, but the ability of a lipid structure to mediate interactions with cellular membranes, we calculated the logP values and found that they did not correlate with uptake efficiency (Figure 3E). Noticeable differences were also found in the localization of lipid-fluorescein conjugates to different cellular membranes. While the overall fluorescence of **3** was stronger than **6**, the latter was found to exclusively localize to ER membranes, while **3** was predominantly localized to the plasma membrane (Figure 3F and G).

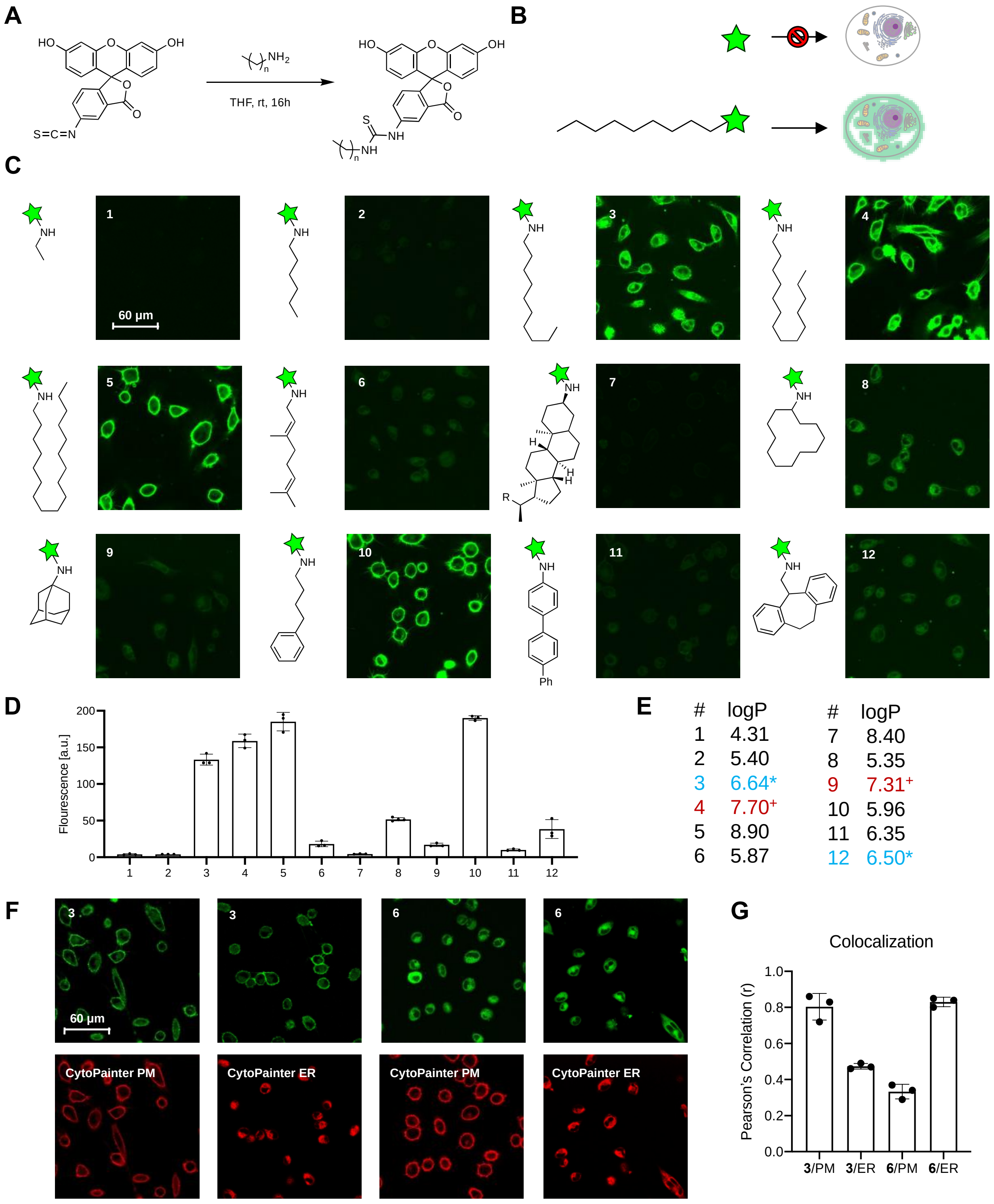

Figure 3 | Cellular uptake and localization of lipid-conjugated fluoresceins. (A) Synthesis of lipid-conjugated fluoresceins. (B) Schematic of lipid-mediated cellular uptake of lipid-conjugated fluoresceins. (C) Confocal images of HeLa cells after 15 min incubation with lipid-conjugated

fluoresceins. All images were acquired under the same experimental conditions. (D) Quantification of fluorescence intensity of cells in (C). (E) Calculations of logP values of lipid-conjugated fluoresceins. Two pairs of logP values are highlighted to illustrate that similar values can lead to very different outcomes for cellular uptake. (F) Colocalization experiment with lipid-conjugated fluoresceins **3** and **6** using plasma membrane and ER localized dyes. (G) Analysis of Pearson's Correlation (r) for the colocalization experiment. Error bars represent SEM.

We next studied the effect of lipid conjugation on molecules that exhibit good cellular permeability to assess if lipid-conjugation could also be detrimental to cellular uptake. Rhodamine-derivatives are thought to exhibit good cellular permeability and rapid cellular accumulation.[44,45] Lipid-rhodamine conjugates were prepared from rhodamine B isothiocyanate (RITC) and aminolipids (Figure 4A). We decided to test a medium-length lipid tail (**C10-Rhodamine**) and a long lipid tail (**C18-Rhodamine**) and a derivative without lipid tail for comparison (**C2-Rhodamine**). Both the non-lipidated analog **C2-Rhodamine** and **C10-Rhodamine** exhibited comparable cellular uptake (Figure 4B and C) indicating that a medium-length lipid tail does not interfere notably with the cellular uptake. Interestingly, **C18-Rhodamine** exhibited markedly reduced cellular uptake suggesting that long lipid tails inhibit the bioavailability of this small molecule scaffold. To test if the rapid uptake within 15 min is following an active or a passive transport mechanism, we used a series of inhibitors of active transport in combination with **C10-Rhodamine** (Figure 4D). Wortmannin is a non-specific PI3K inhibitor that inhibits clathrin-mediated endocytosis,[46] cytochalasin D (CytoD) inhibits actin polymerization affecting many different types of active transport,[47] and chlorpromazine inhibits clathrin-mediated endocytosis through inhibiting the adapter complex AP2.[48] None of these drugs reduced the amount of **C10-Rhodamine** taken up suggesting that uptake may be mediated either through solute carriers (SLCs) or passive diffusion. Unlike the corresponding FITC-conjugate, **C18-Rhodamine** does not associate strongly with the plasma membrane and overall cellular fluorescence is decreased. This points to a separate mechanism that reduces bioavailability and we reasoned that this could be due to a higher propensity to form aggregates. A dynamic light scattering measurement confirmed a lower critical aggregation concentration for **C18-Rhodamine** compared to the other analogs (Figure 4E). This could also potentially contribute to reduced bioactivity of longer lipid-small molecule conjugates.

To expand on the number of small molecule scaffolds, we turned to another fluorophore, which is widely used in live cell imaging, nitrobenzoxadiazole (NBD).[49] NBDs are commonly used for the development of fluorescent lipids and considered membrane-permeable.[50] Lipidation of NBD was achieved through nucleophilic aromatic substitution (S_NAr) of 4-chloro-7-nitrobenzo-2-oxa-1,3-diazole with aminolipids (Figure 4F). Analogously to the lipid-rhodamine series, we decided to conjugate NBD with C2 (**C2-NBD**), C10 (**C10-NBD**), and C18 (**C18-NBD**) saturated lipid tails. Notably, only the medium-length lipid conjugate **C10-NBD** resulted in accumulation in HeLa cells (Figure 4G and H). Both **C2-NBD** and **C18-NBD** were not found to show significant cellular uptake. While the increased uptake of **C10-NBD** compared to **C18-NBD** is consistent with our previous findings, it was surprising that **C2-NBD** was not found to accumulate in cells. To assess the capacity of these conjugates to permeate passively through a phospholipid bilayer, we conducted a parallel artificial membrane permeability assay (PAMPA) experiment (Figure 4I). Interestingly, **C2-NBD** was found to permeate an artificial membrane much more rapidly than both **C10-NBD** and **C18-NBD**, indicating that poor retention could be the primary reason why **C2-NBD** does not accumulate in cells. This highlights another potential advantage of medium-chain lipid tail conjugation, namely the increased cellular retention due to the capacity of lipids to interact with proteins and membranes. Consistent with our previous findings, we found that none of the inhibitors of active cellular transport inhibited the uptake of **C10-NBD** (Figure 4J).

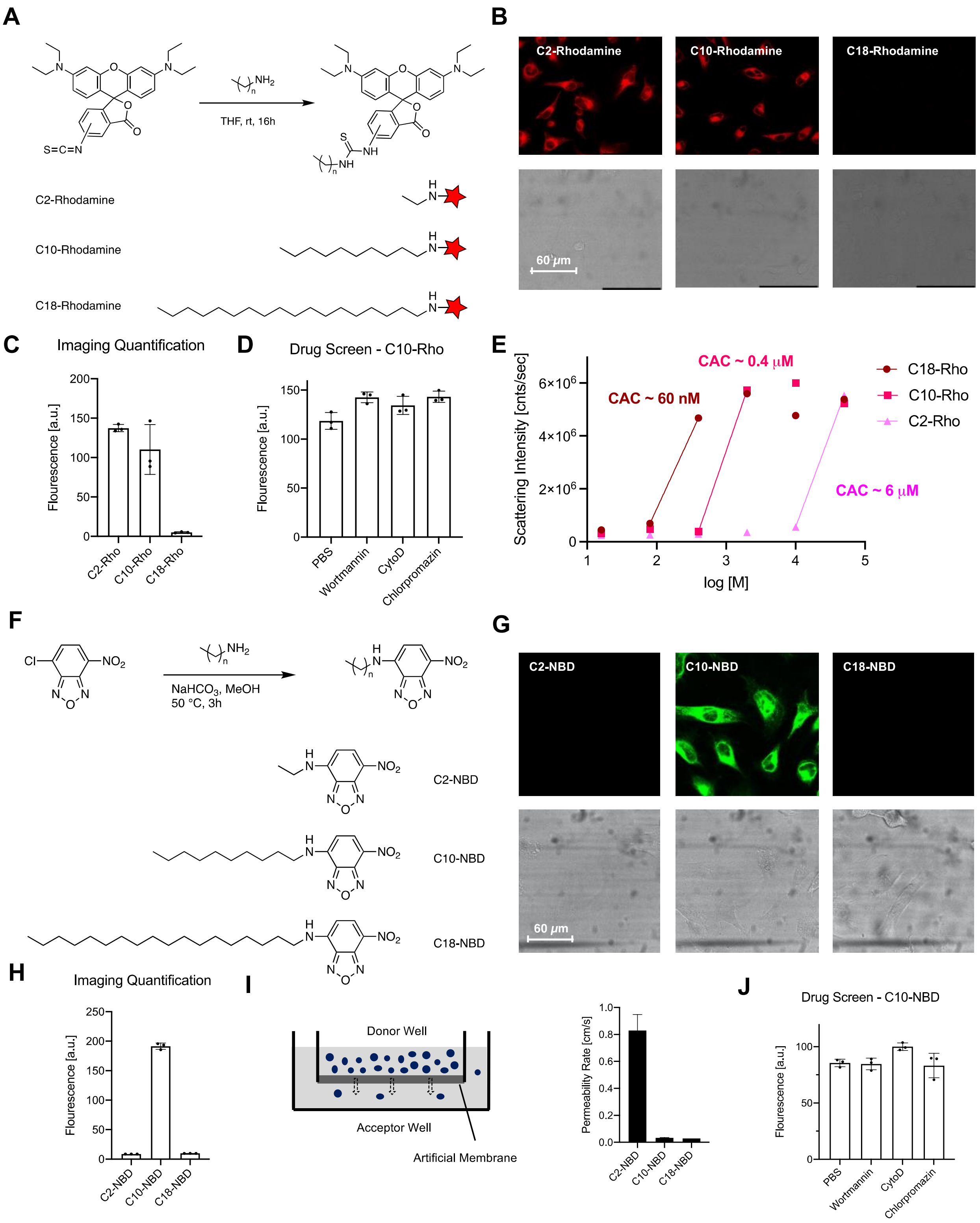

Figure 4 | Cellular uptake of lipid-conjugated rhodamines and NBDs. (A) Synthesis of lipid-conjugated rhodamines and structures of **C2-Rhodamine**, **C10-Rhodamine**, and **C18-Rhodamine**. (B) Confocal images of cellular uptake of lipid-conjugated rhodamines in HeLa cells.

(C) Quantification of uptake in (B). (D) Screen of drugs that inhibit active cellular uptake processes that could be involved in uptake of **C10-Rhodamine**. (E) Dynamic light scattering measurement to determine critical aggregation concentration (CAC). (F) Chemical synthesis of lipid-conjugated NBDs and chemical structures of **C2-NBD**, **C10-NBD**, and **C18-NBD**. (G) Confocal images of lipid-conjugated NBDs in HeLa cells. (H) Quantification of (G). (I) Parallel artificial membrane permeability assay with lipid-conjugated NBDs. (J) Screen of drugs that inhibit active cellular uptake processes that could be involved in uptake of **C10-NBD**. Error bars represent SEM.

Cellular Uptake and Bioactivity of Pharmacophore-Lipid Conjugates

Having established with fluorophores what the most suitable lipid structures are, we next turned our attention to two small molecules with well-known biological effects. Taxol and its derivatives are microtubule stabilizing molecules that have been approved for the treatment of various types of cancer.[51] Due to P-glycoprotein-mediated drug efflux, the delivery of taxol can present a challenge, and various methods have been developed to ensure lasting accumulation in cells.[52] To test if lipid-conjugation could be a suitable platform to increase bioavailability of taxol derivatives, we conjugated docetaxel (DTX) with various lipids. Lipidation could alter the distribution of taxol-conjugates in ways that either attenuate or facilitate drug efflux. Synthesis of lipid conjugates was achieved through Boc-deprotection and subsequent amide-coupling with docetaxel (Figure 5A). We synthesized docetaxel derivatives with C5 (**C5-DTX**), C11 (**C11-DTX**), and C18 (**C18-DTX**) saturated lipid tails and a terminal alkyne. The terminal alkyne could be used for indirect detection of the respective derivatives using copper-catalyzed azide-alkyne cycloaddition (CuAAC) (Figure 5B). We expected that the wash-out of lipid-DTX-fluorophore conjugates occurs more slowly with longer lipids due to increased cellular retention; therefore, the lower fluorescence intensity of **C18-DTX** compared to **C11-DTX** likely reflects reduced cellular uptake of **C18-DTX**. This result is consistent with previous findings that long-chain lipids can present a barrier to the cellular permeability of small molecules. To compare the bioactivity of Lipid-DTX conjugates, we conducted cell viability experiments in two different cancer cell lines, HeLa and MCF7 (Figure 5C) cells. Notably, we found that **C11-DTX** exhibits the greatest cytotoxicity of all three conjugates. While it was found to be slightly more toxic than **C5-DTX**, the toxicity of **C18-DTX** is markedly reduced. It also should be noted that non-conjugated DTX was found to be significantly more toxic than all lipid conjugates. This could be due to increased membrane affinity of these conjugates either leading to drug efflux or reduced availability for microtubule binding, which is one of the few non-membrane bound cellular drug-targets.

We next decided to explore molecules targeting membrane proteins. The quaternary ammonium-based sodium channel blockers QX222 and QX314 are commonly used in neuroscience and lack cellular permeability.[53–55] When applied internally (e.g. through a patch pipette), channel blocking can be observed, while external application to cells does not show any effect.[56] We decided to synthesize a series of analogs without lipid tail (**C0-QX**), with a medium-length lipid tail (**C10-QX**), and with a long lipid tail (**C16-QX**). Lipidated QX-analogs were synthesized through activation of betaine as the acyl chloride and subsequent addition of alkyl-anilines (Figure 5D). We tested this series of QX analogs in NG108.15 cells which express $Na_v1.7$ channels. Currents were recorded in whole cell patch clamp mode upon external application. Notably, we only recorded external Na^+ current blockage with the medium-length lipid conjugate, **C10-QX** (Figure 5E). This suggests that the medium-length tail enables membrane entry leading to the observed bioactivity.

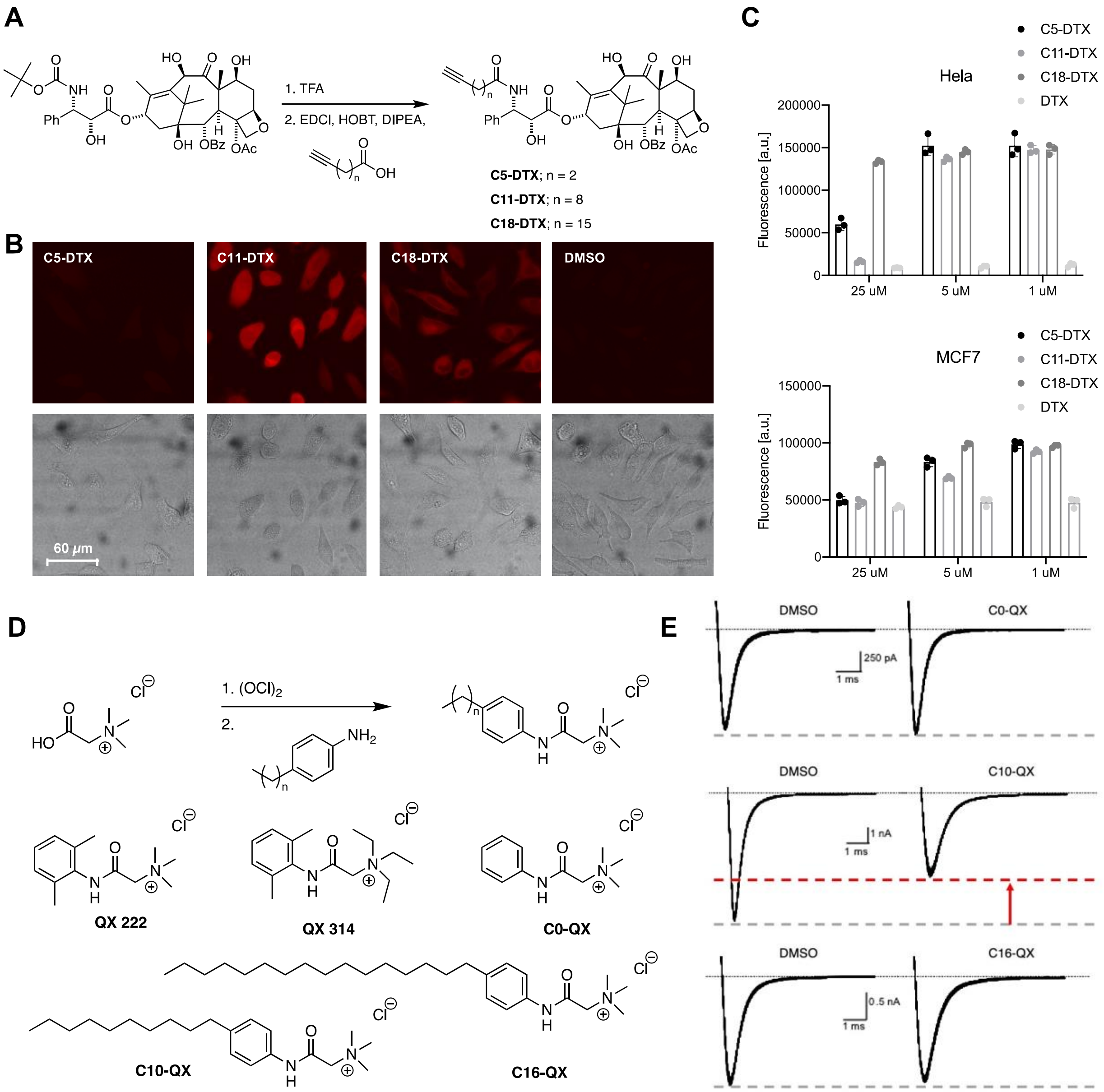

Figure 5 | Synthesis, cellular uptake, and bioactivity of lipid-DTX conjugates and QX-conjugates. (A) Synthesis of lipid-DTX conjugates and chemical structures of lipid-DTX conjugates. (B) Click-imaging after treatment of HeLa cells with lipid-DTX conjugates, fixation, and CuAAC with sulfo-cyanine5 azide. (C) Cellular viability of the cancer cell lines Hela and MCF7 in the presence of lipid-DTX conjugates. Cells were treated for 48 hours and PrestoBlue^{TM} cell viability reagent was used to assess cellular viability after treatment. Error bars represent SEM. (D) Synthesis and chemical structures of lipid-QX conjugates. (E) Representative traces of Na^+ current (200 pulses) in absence (left panel, at 200 pulses) and presence of QX-conjugates (right panel, at 2000 pulses).

Discussion

How small molecules interplay with biological membranes is central to their bioactivity. Molecule-membrane interactions determine cellular uptake, retention, partioning, and accumulation in intracellular compartments. In natural products, bioactive molecules are often conjugated with lipid groups to fine-tune these interactions. Herein, we systematically characterized the types of lipid groups used in natural products, and outlined a strategy to study how different synthetic chemotypes could benefit from such conjugation.

Our chemoinformatic characterization revealed that lipids in secondary metabolites are significantly shorter than those used in the functionalization of proteins or as components of biological membranes. Systematic synthetic lipidation of fluorophores and bioactive small molecules demonstrated how permeability, retention, and bioactivity of small molecules can benefit from this conjugation. Strikingly, we found that saturated medium-length lipids facilitated cellular accumulation and bioactivity of the chemotypes explored. This was especially pronounced for non-permeable molecules like fluorescein or QX-derivatives, where lipid conjugation effectively switched on uptake and bioactivity. This also extended to other chemotypes, where this conjugation was best tolerated compared to longer lipids and even shorter lipids. In many cases, long-chain lipid tails were found to exhibit the reverse effect and hamper cellular uptake and bioactivity. In the case of fluorescein, long-chain conjugates associate readily with the plasma membrane but are less prone to cellular uptake than their medium-length analogs. Other long-chain conjugates do not readily associate with the plasma membrane, which could reflect a higher propensity of longer lipids to self-aggregate. This presents another reason why longer chain lipids are generally less suitable for small molecule conjugation. Our findings on chain-length dependence of cellular uptake and bioactivity are consistent with a recent computational study on the energetic barrier for the translocation of lipidated quorum sensing modulators, finding an energetic minimum for the translocation of medium-length lipids.[57]

Another important finding of this study is the dependence of the described effects on lipid structure. A large screen of lipid fluorescein conjugates revealed that structural differences (e.g. between a floppy saturated lipid and more rigid variants) can be highly consequential for both uptake and even affinities to different types of cellular membranes, while the overall lipophilicity (logP) is comparable. The different preferences for membrane composition could be an interesting mechanism for subcellular targeting which warrants further investigation.

Our systematic analysis of lipidated natural products and functionalization of small molecule scaffolds suggests that conjugation of lipid tails could be a useful design principle for probes and pharmacophores. Nature has used this modification extensively to fine-tune the bioactivity of natural products and it has chosen saturated medium-length lipids for this purpose. Our data suggests that this modification should be broadly applied to improve the bioavailability of pharmacophores and probes.

Experimental Section

General Methods. All reagents and solvents were purchased from commercial sources (Sigma-Aldrich, TCI Europe N.V., Strem Chemicals, etc.) and were used without further purification. Solvents were obtained from Fisher Scientific. Reactions were monitored by thin layer chromatography (TLC) on pre-coated, Merck Silica gel 60 F_{254} aluminum-backed plates and the chromatograms were first visualized by UV irradiation at λ = 254 nm. Flash silica gel chromatography was performed using silica gel (SiO_2, particle size 40-63 μm) purchased from SiliCycle. NMR spectra were measured on a BRUKER Avance III HD 400 (equipped with a CryoProbe^{TM}). Multiplicities in the following experimental procedures are abbreviated as follows: s = singlet, d = doublet, t = triplet, q = quartet, m = multiplet. ^{1}H chemical shifts are expressed in parts per million (ppm, δ scale) and are referenced to the residual protium in the NMR solvent ($CDCl_3$: δ = 7.26; MeOH: δ = 3.31). ^{13}C chemical shifts are expressed in ppm (δ scale) and are referenced to the carbon resonance of the NMR solvent ($CDCl_3$: δ = 77.16, MeOH: δ = 49.00).

General procedure for synthesis of lipid-conjugated fluoresceins

Fluorescein 5-isothiocyanate (15.0 mg, 38.5 μmol, 1.0 equiv.) was dissolved in THF (1 mL) in a 20 mL glass vial. Aminolipid (46.2 μmol, 1.2 equiv.) was added and stirred for 16 h at room temperature. Solvents were removed under reduced pressure and the residue was purified by silica flash column chromatography ($CH_2Cl_2 \rightarrow$ MeOH:CH_2Cl_2 1:4) to yield the product as orange solid.

General procedure for synthesis of lipid-conjugated rhodamines

Rhodamine 5(6)-isothiocyanate (20.7 mg, 38.5 μmol, 1.0 equiv.) was dissolved in THF (1 mL) in a 20 mL glass vial. Aminolipid (46.2 μmol, 1.2 equiv.) was added and stirred for 16 h at room temperature. Solvents were removed under reduced pressure and the residue was purified by silica flash column chromatography (CH_2Cl_2 → MeOH:CH_2Cl_2 1:4) to yield the product as pink solid.

General procedure for synthesis of lipid-conjugated NBDs

Aminolipid (150 μmol, 1.0 equiv.) was dissolved in MeOH (1 mL) in a 20 mL glass vial. 4-chloro-7-nitrobenzo-2-oxa-1,3-diazole (30.0 mg, 150 μmol, 1.0 equiv.) and $NaHCO_3$ (37.9 mg, 451 μmol, 3.0 equiv.) were added and stirred at 50 °C for 3 h. MeOH was removed under reduced pressure, water was added, and acidified with 1 M HCl. The aqueous phase was extracted with EtOAc and the organic phase was dried over Na_2SO_4, filtered, and concentrated under reduced pressure. The residue was purified by silica flash column chromatography (hexanes → EtOAc:hexanes 1:1) to yield the product as red solid.

General procedure for synthesis of lipid-conjugated taxols

Docetaxel (33.0 mg, 40.8 μmol, 1.0 equiv.) was dissolved in CH_2Cl_2 (1 mL) in a 20 mL glass vial. TFA (1 mL) was added at 0 °C and stirred for 1 h. Sat. aqueous $NaHCO_3$ was added to neutralize and extracted with CH_2Cl_2, washed with brine, dried over Na_2SO_4, filtered, and concentrated under reduced pressure. Lipid was dissolved in DMF (0.5 mL) in a separate 20 mL glass vial. HOBt (15.6 mg, 102 μmol, 2.5 equiv.) and EDC (17.6 mg, 91.9 μmol, 2.2 equiv.) were added. A solution of DIPEA (21.1 mg, 163 μmol, 4.0 equiv.) in DMF (0.5 mL) was added. Crude mixture of deprotected docetaxel was added in DMF (0.5 mL) and stirred for 16 h at room temperature. Volatiles were removed under reduced pressure and the residue was purified by silica flash column chromatography (CH_2Cl_2 → MeOH:CH_2Cl_2 1:9) to yield the product as colorless solid.

General procedure for synthesis of lipid-conjugated QX

Betaine (20.0 mg, 169 μmol, 1.0 equiv.) was suspended in DMF (1 mL) in a 20 mL glass vial. Aniline (203 μmol, 1.2 equiv.), TBTU (65.2 mg, 203 μmol, 1.2 equiv.), and DIPEA (52.5 mg, 406 μmol, 2.4 equiv.) were added and stirred for 16 h at room temperature. The solution was filtered and purified by HPLC to yield the product as colorless solid.

Live cell imaging of lipid-fluorophore conjugates

HeLa cells were plated on a poly-lysine pre-coated 8-well imaging dish at a density of 25k cells per well. After overnight incubation at 37 °C and 5% CO_2, the medium was removed and lipid fluorophore conjugates were added as 10 μM solution in PBS at a final concentration of 0.2 % DMSO for 15 min. The cells were washed twice with PBS and directly imaged on a Leica DMI6000B inverted confocal microscope equipped with a Leica HC PL APO 63x/1.30 Flyc CORR CS2 immersion objective and a Leica TCS SP8 X white laser.

Dynamic Light Scattering

Measurements were performed using a DynaPro MS/X (Wyatt Technology) with a 55 mW laser at 826.6 nm, using a detector angle of 90°. Histograms represent the average of three data sets.

Parallel artificial membrane permeability assay (PAMPA)

PAMPA assays were measured with a bioassay systems kit (PAMPA-096) following the vendor's protocol.

Cell Viability Assay

Hela or MCF7 cells were seeded in a 96 well plate (approx. 10k per well in 100 μL) in DMEM/FCS/PS (90:10:1). After 24 h, 100 μL of 2x solution of compound in DMEM/FCS/PS (90:10:1) and 2% DMSO was added. After 48 h of compound incubation PrestoBlue (Thermo Scientific) was added (20 μL per well) and after 2h fluorescence was measured using a BMG Labtech FLUOstar Omega microplate reader with 544/590 nm filters.

Electrophysiology

NG108-15 cells were purchased from ATCC (Manassas, VA) and maintained in culture in DMEM media (without sodium pyruvate, Gibco, Thermo Fischer Scientific) supplemented with (in mmole/L): 0.1 hypoxanthine, 0.016 thymidine, 10% FBS and 5 ml Pen/Strep solution. Cells were grown in 100 mm culture plates until 70-80% confluence before plating cells on 12 mm glass coverslips for electrophysiology recordings. Membrane currents were recorded using the whole cell membrane patch configuration at room temperature using an Axopatch 200B amplifier (Molecular Devices, San Jose, CA). Currents were filtered at 5 kHz and data acquired at 10 kHz (Digidata 1550A and Clampex 10; Molecular Devices). Patch pipettes were made with borosilicate glass (1.5mm OD; World Precision Instruments, Sarasota, FL) and had resistances of ~3 MΩ when filled with pipette solution consisting of (in mmole/L) 50 CsCl, 10 NaCl, 60 Cs-fluoride, 20 EGTA, 10 HEPES, and pH 7.2 with CsOH (285 mOsm). The bath solution consisted of (in mmole/L) 140 NaCl, 5 KCl, 2 $MgCl_2$, 1 $CaCl_2$, 10 HEPES, 10 glucose and pH 7.2 with TEA-OH (300 mOsm). Pipette capacitances were fully compensated and cell capacitances and series resistances were compensated. Na currents were evoked by applying 200 depolarizing pulses (10 ms in duration) from a holding potential of -120 mV to -10 mV at 10 Hz. Recordings were made before and after extracellular application of QX-analogs (100 µM each). A minimum of three recordings were made in each group.

COCONUT database preprocessing

The coconut database was downloaded, and its 400,837 entries were filtered down to the 67,730 structures having taxonomical annotation and a DOI annotation not shorter than 10 characters. MW, Fsp3, HBD, and HBA count, and the LogP calculated following the Crippen[58] method (AlogP) were calculated using RDKit.[59] Molecules breaking more than one Lipinski's rule[36] were labeled as non-Lipinski. The presence/absence of a peptide or a glycoside moiety was evaluated using Daylight[60] SMILES arbitrary target specification (SMARTS) language and RDKit. The glycoside substructure was defined as a cyclic N- or O-acetal substructure. The plant, fungal, bacterial, animal, marine, or human origin of the natural products was extrapolated from the COCONUT taxonomy annotation. If belonging to more than one class, the entry was with the priority: human > animal > bacteria > fungi > plant > marine. The processes resulted in 33,821 plants NPs, 15,693 fungal NPs, 10,819 bacterial NPs, 1,779 human NPs, 1,219 animal NPs, 1,035 marine NPs, and 3,364 NPs missing a super classification labelled as “other”.

Lipidated natural products identification

Within this analysis, lipidated natural products were selected following four criteria: (i) the presence of a terminal eight carbons long aliphatic chain, (ii) the presence of at least one non-carbohydrate ring, (iii) the presence of a non-lipidic and non-carbohydrate core of at least 200 Da (iv), and the absence of a sterol substructure. The presence of a terminal eight carbons long aliphatic chain was determined with RDKit using the Daylight SMARTS language. To assess if terminal, the lipidic chain substructure was identified through SMARTS and removed, and the length of the SMILES of the remaining fragments was calculated. When only one of the remaining fragments had a SMILES length of more than ten characters, the chain was considered terminal. Non-carbohydrates rings were counted using RDKit and the “sugar free SMILES” annotated in COCONUT. To assess the MW of the non-lipidic and non-carbohydrate core, the lipid chain substructure was identified through SMARTS and removed from the COCONUT “sugar free” SMILES, and the MW of the remaining largest fragment was calculated. The absence of sterol substructure was evaluated using Daylight SMARTS language with RDKit. The selection led to 1,390 lipidated natural products, which were further filtered down manually to 1,308 structures.

Lipidated natural products characterization

The 1,308 structures were characterized based on their origin, lipidic linker, and the length and unsaturation level of their longest lipidic chain. The lipidic linker was classified as amide, esters, ether, or amine using Daylight SMARTS language and RDKit. The origin of the natural products was obtained as described above. The unsaturation number was calculated by counting the number of double and triple bonds in the longest lipidic chain. The fraction of unsaturation was calculated by doubling the number of unsaturation and dividing it by the number of atoms present in the longest lipidic chain. The lipidic chains were identified as described above, and the number of unsaturation and atoms was calculated using RDKit.

TMAP generation

TMAP was used to visualize the 67,730 entries COCONUT subset. MAP4 was calculated using the related open-source code. The indices generated by the MinHash procedure of the MAP4 calculation were used to create a 32 trees locality-sensitive hashing (LSH) forest.[61] Then, for each structure to display, the 20 approximate nearest neighbors (NNs) were obtained from the LSH forest, and the TMAP minimum spanning tree layout was calculated. The LSH forest and the minimum spanning tree layout were calculated using the TMAP open-source code. Finally, Fearun[35] was used to display the obtained tree layout interactively. The MW, Fsp3, HBD and HBA count, AlogP, taxonomical origin, presence/absence of a peptidic substructure, presence/absence of a glycoside substructure, the Lipinski classification, and the lipidation of the displayed structures were used to color code the interactive TMAP.

Data availability

The code used to analyze and visualize the lipidated NPs in COCONUT can be found at https://github.com/reymond-group/LipidatedNPs

Associated Content

Supporting Information. Additional TMAPs for lipidated NPs. Chemical synthesis and characterization.

Author Information

Corresponding Authors

*johannes.morstein@ucsf.edu

Notes

The author declares no competing financial interests.

Author Contributions

#These authors contributed equally.

Acknowledgments

J. M. thanks the NCI for a K00 award (4K00CA253758). We acknowledge the NYU Langone Health's Ion Laboratory for conducting electrophysiology experiments. Support for the IonLab is partially provided through the Office of Scientific Research, NIH RO1 AI097302, NIH sub award D009105901 and Nanion Technologies Inc. We thank Joe O'Connell from Brian Shoichet's lab for assistance with the DLS measurement. We thank Dr. Kevan M. Shokat, Dr. Paramjit Arora, Dr. D. Matthew Peacock, Dr. Ziyang Zhang, Kevin Lou, Siyi Wang for critical comments and helpful discussion.

References

(1) Sugano, K.; Kansy, M.; Artursson, P.; Avdeef, A.; Bendels, S.; Di, L.; Ecker, G. F.; Faller, B.; Fischer, H.; Gerebtzoff, G.; Lennernaes, H.; Senner, F. Coexistence of Passive and Carrier-Mediated Processes in Drug Transport. *Nat. Rev. Drug Discov.* **2010**, *9* (8), 597–614. https://doi.org/10.1038/nrd3187.

(2) Naylor, M. R.; Ly, A. M.; Handford, M. J.; Ramos, D. P.; Pye, C. R.; Furukawa, A.; Klein, V. G.; Noland, R. P.; Edmondson, Q.; Turmon, A. C.; Hewitt, W. M.; Schwochert, J.; Townsend, C. E.; Kelly, C. N.; Blanco, M.-J.; Lokey, R. S. Lipophilic Permeability Efficiency Reconciles the Opposing Roles of Lipophilicity in Membrane Permeability and Aqueous Solubility. *J. Med. Chem.* **2018**, *61* (24), 11169–11182. https://doi.org/10.1021/acs.jmedchem.8b01259.

(3) Shultz, M. D. Two Decades under the Influence of the Rule of Five and the Changing Properties of Approved Oral Drugs. *J. Med. Chem.* **2019**, *62* (4), 1701–1714. https://doi.org/10.1021/acs.jmedchem.8b00686.

(4) Brinkmann, V.; Billich, A.; Baumruker, T.; Heining, P.; Schmouder, R.; Francis, G.; Aradhye, S.; Burtin, P. Fingolimod (FTY720): Discovery and Development of an Oral Drug to Treat Multiple Sclerosis. *Nat. Rev. Drug Discov.* **2010**, *9* (11), 883–897. https://doi.org/10.1038/nrd3248.

(5) Shayman, J. A. ELIGLUSTAT TARTRATE. *Drugs Future* **2010**, *35* (8), 613–620.

(6) Dekker, F. J.; Rocks, O.; Vartak, N.; Menninger, S.; Hedberg, C.; Balamurugan, R.; Wetzel, S.; Renner, S.; Gerauer, M.; Schölermann, B.; Rusch, M.; Kramer, J. W.; Rauh, D.; Coates, G. W.; Brunsveld, L.; Bastiaens, P. I. H.; Waldmann, H. Small-Molecule Inhibition of APT1 Affects Ras Localization and Signaling. *Nat. Chem. Biol.* **2010**, *6* (6), 449–456. https://doi.org/10.1038/nchembio.362.

(7) Johnson, M. Salmeterol. *Med. Res. Rev.* **1995**, *15* (3), 225–257. https://doi.org/10.1002/med.2610150303.

(8) Ortar, G.; Bisogno, T.; Ligresti, A.; Morera, E.; Nalli, M.; Di Marzo, V. Tetrahydrolipstatin Analogues as Modulators of Endocannabinoid 2-Arachidonoylglycerol Metabolism. *J. Med. Chem.* **2008**, *51* (21), 6970–6979. https://doi.org/10.1021/jm800978m.

(9) Wender, P. A.; Hinkle, K. W. Synthesis and Biological Evaluation of a New Class of Bryostatin Analogues: The Role of the C20 Substituent in Protein Kinase C Binding. *Tetrahedron Lett.* **2000**, *41* (35), 6725–6729. https://doi.org/10.1016/S0040-4039(00)01100-X.

(10) Wender, P. A.; Hardman, C. T.; Ho, S.; Jeffreys, M. S.; Maclaren, J. K.; Quiroz, R. V.; Ryckbosch, S. M.; Shimizu, A. J.; Sloane, J. L.; Stevens, M. C. Scalable Synthesis of Bryostatin 1 and Analogs, Adjuvant Leads against Latent HIV. *Science* **2017**, *358* (6360), 218–223. https://doi.org/10.1126/science.aan7969.

(11) Chu, H.; Dünstl, G.; Felding, J.; Baran, P. S. Divergent Synthesis of Thapsigargin Analogs. *Bioorg. Med. Chem. Lett.* **2018**, *28* (16), 2705–2707. https://doi.org/10.1016/j.bmcl.2018.03.065.

(12) Schneider, E. K.; Huang, J. X.; Carbone, V.; Han, M.; Zhu, Y.; Nang, S.; Khoo, K. K.; Mak, J.; Cooper, M. A.; Li, J.; Velkov, T. Plasma Protein Binding Structure–Activity Relationships Related to the N-Terminus of Daptomycin. *ACS Infect. Dis.* **2017**, *3* (3), 249–258. https://doi.org/10.1021/acsinfecdis.7b00015.

(13) Wada, R.; Suto, Y.; Kanai, M.; Shibasaki, M. Dramatic Switching of Protein Kinase C Agonist/Antagonist Activity by Modifying the 12-Ester Side Chain of Phorbol Esters. *J. Am. Chem. Soc.* **2002**, *124* (36), 10658–10659. https://doi.org/10.1021/ja027048s.

(14) Mason, R. P.; Rhodes, D. G.; Herbette, L. G. Reevaluating Equilibrium and Kinetic Binding Parameters for Lipophilic Drugs Based on a Structural Model for Drug Interactions with Biological Membranes. *J. Med. Chem.* **1991**, *34* (3), 869–877. https://doi.org/10.1021/jm00107a001.

(15) Vauquelin, G.; Packeu, A. Ligands, Their Receptors and … Plasma Membranes. *Mol. Cell. Endocrinol.* **2009**, *311* (1), 1–10. https://doi.org/10.1016/j.mce.2009.07.022.

(16) Payandeh, J.; Volgraf, M. Ligand Binding at the Protein–Lipid Interface: Strategic Considerations for Drug Design. *Nat. Rev. Drug Discov.* **2021**, 1–13. https://doi.org/10.1038/s41573-021-00240-2.

(17) Overington, J. P.; Al-Lazikani, B.; Hopkins, A. L. How Many Drug Targets Are There? *Nat Rev Drug Discov* **2006**, *5* (12), 993–996. https://doi.org/10.1038/nrd2199.

(18) Stanley, N.; Pardo, L.; Fabritiis, G. D. The Pathway of Ligand Entry from the Membrane Bilayer to a Lipid G Protein-Coupled Receptor. *Sci. Rep.* **2016**, *6* (1), 22639. https://doi.org/10.1038/srep22639.

(19) Sutcliffe, K. J.; Corey, R. A.; Charlton, S. J.; Sessions, R. B.; Henderson, G.; Kelly, E. *Fentanyl Binds to the μ-Opioid Receptor via the Lipid Membrane and Transmembrane Helices*; 2021; p 2021.02.04.429703. https://doi.org/10.1101/2021.02.04.429703.

(20) Tian, H.; Gunnison, K. M.; Kazmi, M. A.; Sakmar, T. P.; Huber, T. *Entry Pathway for the Inverse Agonist Ligand in the G Protein-Coupled Receptor Rhodopsin*; 2021; p 2021.05.24.445474. https://doi.org/10.1101/2021.05.24.445474.

(21) Szlenk, C. T.; Gc, J. B.; Natesan, S. Does the Lipid Bilayer Orchestrate Access and Binding of Ligands to Transmembrane Orthosteric/Allosteric Sites of G Protein-Coupled Receptors? *Mol. Pharmacol.* **2019**, *96* (5), 527–541. https://doi.org/10.1124/mol.118.115113.

(22) Dong, Y. Y.; Pike, A. C. W.; Mackenzie, A.; McClenaghan, C.; Aryal, P.; Dong, L.; Quigley, A.; Grieben, M.; Goubin, S.; Mukhopadhyay, S.; Ruda, G. F.; Clausen, M. V.; Cao, L.; Brennan, P. E.; Burgess-Brown, N. A.; Sansom, M. S. P.; Tucker, S. J.; Carpenter, E. P. K2P Channel Gating Mechanisms Revealed by Structures of TREK-2 and a Complex with Prozac. *Science* **2015**, *347* (6227), 1256–1259. https://doi.org/10.1126/science.1261512.

(23) Villemure, E.; Terrett, J. A.; Larouche-Gauthier, R.; Déry, M.; Chen, H.; Reese, R. M.; Shields, S. D.; Chen, J.; Magnuson, S.; Volgraf, M. A Retrospective Look at the Impact of

Binding Site Environment on the Optimization of TRPA1 Antagonists. *ACS Med. Chem. Lett.* **2021**, *12* (8), 1230–1237. https://doi.org/10.1021/acsmedchemlett.1c00305.

(24) Wenk, M. R. The Emerging Field of Lipidomics. *Nat. Rev. Drug Discov.* **2005**, *4* (7), 594–610. https://doi.org/10.1038/nrd1776.

(25) Shevchenko, A.; Simons, K. Lipidomics: Coming to Grips with Lipid Diversity. *Nat. Rev. Mol. Cell Biol.* **2010**, *11* (8), 593–598. https://doi.org/10.1038/nrm2934.

(26) Hang, H. C.; Linder, M. E. Exploring Protein Lipidation with Chemical Biology. *Chem. Rev.* **2011**, *111* (10), 6341–6358. https://doi.org/10.1021/cr2001977.

(27) Jiang, H.; Zhang, X.; Chen, X.; Aramsangtienchai, P.; Tong, Z.; Lin, H. Protein Lipidation: Occurrence, Mechanisms, Biological Functions, and Enabling Technologies. *Chem. Rev.* **2018**, *118* (3), 919–988. https://doi.org/10.1021/acs.chemrev.6b00750.

(28) Avadisian, M.; Gunning, P. T. Extolling the Benefits of Molecular Therapeutic Lipidation. *Mol. Biosyst.* **2013**, *9* (9), 2179–2188. https://doi.org/10.1039/c3mb70147f.

(29) Pai, E. F.; Krengel, U.; Petsko, G. A.; Goody, R. S.; Kabsch, W.; Wittinghofer, A. Refined Crystal Structure of the Triphosphate Conformation of H-Ras P21 at 1.35 A Resolution: Implications for the Mechanism of GTP Hydrolysis. *EMBO J.* **1990**, *9* (8), 2351–2359.

(30) Bank, R. P. D. RCSB PDB - 3N1R: Crystal Structure of ShhN https://www.rcsb.org/structure/3n1r (accessed 2021 -08 -16).

(31) Sorokina, M.; Merseburger, P.; Rajan, K.; Yirik, M. A.; Steinbeck, C. COCONUT Online: Collection of Open Natural Products Database. *J. Cheminformatics* **2021**, *13* (1), 2. https://doi.org/10.1186/s13321-020-00478-9.

(32) Capecchi, A.; Reymond, J.-L. Classifying Natural Products from Plants, Fungi or Bacteria Using the COCONUT Database and Machine Learning. *J. Cheminformatics* **2021**, *13* (1), 82. https://doi.org/10.1186/s13321-021-00559-3.

(33) Capecchi, A.; Probst, D.; Reymond, J.-L. One Molecular Fingerprint to Rule Them All: Drugs, Biomolecules, and the Metabolome. *J. Cheminformatics* **2020**, *12* (1), 43. https://doi.org/10.1186/s13321-020-00445-4.

(34) Probst, D.; Reymond, J.-L. Visualization of Very Large High-Dimensional Data Sets as Minimum Spanning Trees. *ArXiv190810410 Cs* **2020**.

(35) Probst, D.; Reymond, J.-L.; Wren, J. FUn: A Framework for Interactive Visualizations of Large, High-Dimensional Datasets on the Web. *Bioinformatics* **2018**, *34* (8), 1433–1435. https://doi.org/10.1093/bioinformatics/btx760.

(36) Lipinski, C. A.; Lombardo, F.; Dominy, B. W.; Feeney, P. J. Experimental and Computational Approaches to Estimate Solubility and Permeability in Drug Discovery and Development Settings. *Adv. Drug Deliv. Rev.* **1997**, *23* (1), 3–25. https://doi.org/10.1016/S0169-409X(96)00423-1.

(37) Jiang, H.; Zhang, X.; Chen, X.; Aramsangtienchai, P.; Tong, Z.; Lin, H. Protein Lipidation: Occurrence, Mechanisms, Biological Functions, and Enabling Technologies. *Chem. Rev.* **2018**, *118* (3), 919–988. https://doi.org/10.1021/acs.chemrev.6b00750.

(38) O'Donnell, V. B.; Dennis, E. A.; Wakelam, M. J. O.; Subramaniam, S. LIPID MAPS: Serving the next Generation of Lipid Researchers with Tools, Resources, Data, and Training. *Sci. Signal.* **2019**, *12* (563), eaaw2964. https://doi.org/10.1126/scisignal.aaw2964.

(39) Bang, E.-K.; Gasparini, G.; Molinard, G.; Roux, A.; Sakai, N.; Matile, S. Substrate-Initiated Synthesis of Cell-Penetrating Poly(Disulfide)s. *J. Am. Chem. Soc.* **2013**, *135* (6), 2088–2091. https://doi.org/10.1021/ja311961k.

(40) Gasparini, G.; Sargsyan, G.; Bang, E.-K.; Sakai, N.; Matile, S. Ring Tension Applied to Thiol-Mediated Cellular Uptake. *Angew. Chem. Int. Ed.* **2015**, *54* (25), 7328–7331. https://doi.org/10.1002/anie.201502358.

(41) Lättig-Tünnemann, G.; Prinz, M.; Hoffmann, D.; Behlke, J.; Palm-Apergi, C.; Morano, I.; Herce, H. D.; Cardoso, M. C. Backbone Rigidity and Static Presentation of Guanidinium

Groups Increases Cellular Uptake of Arginine-Rich Cell-Penetrating Peptides. *Nat. Commun.* **2011**, *2* (1), 453. https://doi.org/10.1038/ncomms1459.

(42) Stanzl, E. G.; Trantow, B. M.; Vargas, J. R.; Wender, P. A. Fifteen Years of Cell-Penetrating, Guanidinium-Rich Molecular Transporters: Basic Science, Research Tools, and Clinical Applications. *Acc. Chem. Res.* **2013**, *46* (12), 2944–2954. https://doi.org/10.1021/ar4000554.

(43) Qian, Z.; Martyna, A.; Hard, R. L.; Wang, J.; Appiah-Kubi, G.; Coss, C.; Phelps, M. A.; Rossman, J. S.; Pei, D. Discovery and Mechanism of Highly Efficient Cyclic Cell-Penetrating Peptides. *Biochemistry* **2016**, *55* (18), 2601–2612. https://doi.org/10.1021/acs.biochem.6b00226.

(44) Johnson, L. V.; Walsh, M. L.; Chen, L. B. Localization of Mitochondria in Living Cells with Rhodamine 123. *Proc. Natl. Acad. Sci. U. S. A.* **1980**, *77* (2), 990–994.

(45) Paul, A.; Mengji, R.; Bera, M.; Ojha, M.; Jana, A.; Singh, N. D. P. Mitochondria-Localized in Situ Generation of Rhodamine Photocage with Fluorescence Turn-on Enabling Cancer Cell-Specific Drug Delivery Triggered by Green Light. *Chem. Commun.* **2020**, *56* (60), 8412–8415. https://doi.org/10.1039/D0CC03524F.

(46) Spiro, D. J.; Boll, W.; Kirchhausen, T.; Wessling-Resnick, M. Wortmannin Alters the Transferrin Receptor Endocytic Pathway in Vivo and in Vitro. *Mol. Biol. Cell* **1996**, *7* (3), 355–367.

(47) Casella, J. F.; Flanagan, M. D.; Lin, S. Cytochalasin D Inhibits Actin Polymerization and Induces Depolymerization of Actin Filaments Formed during Platelet Shape Change. *Nature* **1981**, *293* (5830), 302–305. https://doi.org/10.1038/293302a0.

(48) Wang, L. H.; Rothberg, K. G.; Anderson, R. G. Mis-Assembly of Clathrin Lattices on Endosomes Reveals a Regulatory Switch for Coated Pit Formation. *J. Cell Biol.* **1993**, *123* (5), 1107–1117. https://doi.org/10.1083/jcb.123.5.1107.

(49) Ghosh, P. B.; Whitehouse, M. W. 7-Chloro-4-Nitrobenzo-2-Oxa-1,3-Diazole: A New Fluorigenic Reagent for Amino Acids and Other Amines. *Biochem. J.* **1968**, *108* (1), 155–156. https://doi.org/10.1042/bj1080155.

(50) Chattopadhyay, A. Chemistry and Biology of N-(7-Nitrobenz-2-Oxa-1,3-Diazol-4-Yl)-Labeled Lipids: Fluorescent Probes of Biological and Model Membranes. *Chem. Phys. Lipids* **1990**, *53* (1), 1–15. https://doi.org/10.1016/0009-3084(90)90128-e.

(51) Weaver, B. A. How Taxol/Paclitaxel Kills Cancer Cells. *Mol. Biol. Cell* **2014**, *25* (18), 2677–2681. https://doi.org/10.1091/mbc.E14-04-0916.

(52) Dubikovskaya, E. A.; Thorne, S. H.; Pillow, T. H.; Contag, C. H.; Wender, P. A. Overcoming Multidrug Resistance of Small-Molecule Therapeutics through Conjugation with Releasable Octaarginine Transporters. *Proc. Natl. Acad. Sci. U. S. A.* **2008**, *105* (34), 12128–12133. https://doi.org/10.1073/pnas.0805374105.

(53) Sunami, A.; Dudley, S. C.; Fozzard, H. A. Sodium Channel Selectivity Filter Regulates Antiarrhythmic Drug Binding. *Proc. Natl. Acad. Sci.* **1997**, *94* (25), 14126–14131. https://doi.org/10.1073/pnas.94.25.14126.

(54) Binshtok, A. M.; Bean, B. P.; Woolf, C. J. Inhibition of Nociceptors by TRPV1-Mediated Entry of Impermeant Sodium Channel Blockers. *Nature* **2007**, *449* (7162), 607–610. https://doi.org/10.1038/nature06191.

(55) Wang, Q.; Zhang, Y.; Liu, J.; Zhang, W. <p>Quaternary Lidocaine Derivatives: Past, Present, and Future</P>. *Drug Des. Devel. Ther.* **2021**, *15*, 195–207. https://doi.org/10.2147/DDDT.S291229.

(56) Mourot, A.; Fehrentz, T.; Le Feuvre, Y.; Smith, C. M.; Herold, C.; Dalkara, D.; Nagy, F.; Trauner, D.; Kramer, R. H. Rapid Optical Control of Nociception with an Ion-Channel Photoswitch. *Nat. Methods* **2012**, *9* (4), 396–402. https://doi.org/10.1038/nmeth.1897.

(57) Jin, T.; Patel, S. J.; Lehn, R. C. V. Molecular Simulations of Lipid Membrane Partitioning and Translocation by Bacterial Quorum Sensing Modulators. *PLOS ONE* **2021**, *16* (2), e0246187. https://doi.org/10.1371/journal.pone.0246187.

(58) Wildman, S. A.; Crippen, G. M. Prediction of Physicochemical Parameters by Atomic Contributions. *J. Chem. Inf. Comput. Sci.* **1999**, *39* (5), 868–873. https://doi.org/10.1021/ci990307l.

(59) RDKit https://www.rdkit.org/.

(60) Daylight https://www.daylight.com/ (accessed 2020 -07 -17).

(61) Bawa, M.; Condie, T.; Ganesan, P. LSH Forest: Self-Tuning Indexes for Similarity Search. In *Proceedings of the 14th international conference on World Wide Web*; WWW ’05; Association for Computing Machinery: Chiba, Japan, 2005; pp 651–660. https://doi.org/10.1145/1060745.1060840.

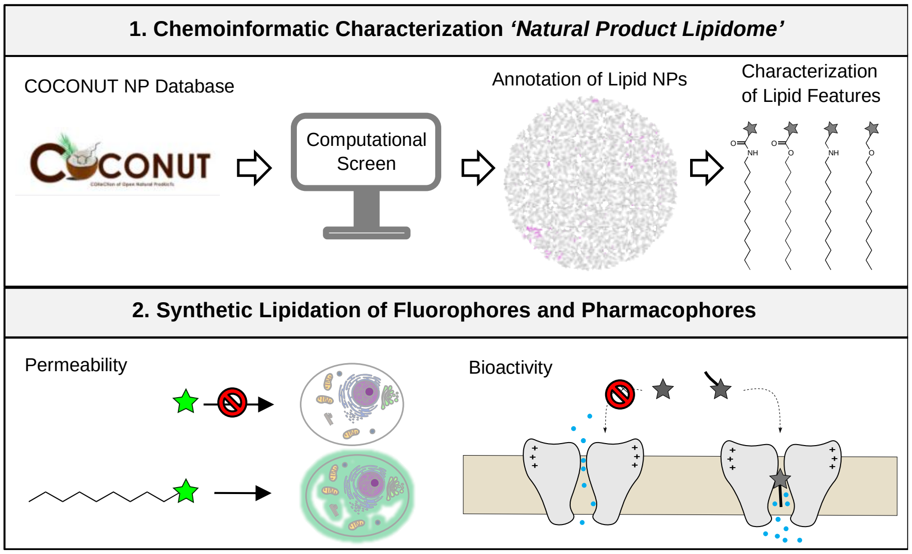
1. Chemoinformatic Characterization 'Natural Product Lipidome'
COCONUT NP Database
COCONUT
Computational Screen
Annotation of Lipid NPs
Characterization of Lipid Features
O
NH
O
O
NH
O
2. Synthetic Lipidation of Fluorophores and Pharmacophores
Permeability
Bioactivity
+
+
+

TOC Figure